PHYSICAL REVIEW B **76**, 094109 (2007)

Recrystallization kinetics: A coupled coarse-grained dislocation density and phase-field approach

S. Sreekala[1,*] and Mikko Haataja[1,2,†]

[1]*Department of Mechanical and Aerospace Engineering, Princeton University, Princeton, New Jersey 08544, USA*

[2]*Princeton Institute for the Science and Technology of Materials (PRISM), Princeton University, Princeton, New Jersey 08544, USA*

(Received 2 February 2007; revised manuscript received 27 May 2007; published 14 September 2007)

During recrystallization, dislocation-poor grains grow and invade the heavily deformed dislocation-rich matrix. In this work, we develop a coupled dislocation density and phase-field method to model the isothermal recrystallization process as a phase transformation, driven by the stored elastic energy. Dislocations are represented in two spatial dimensions in terms of a continuous Burgers vector field, and their contribution to the elastic energy density is explicitly incorporated. A key feature of our approach is that the driving force for grain growth becomes nonlocal in space due to the presence of long-ranged dislocation strain fields. We employ the model to examine the influence of various spatially heterogeneous dislocation distributions (random, cellular, and algebraically correlated) on the growth morphology of an isolated recrystallized grain. Our results show that grain growth can be highly anisotropic and irregular in cellular dislocation networks, in agreement with recent experiments. The source of this anisotropy is related to the anisotropy of the underlying dislocation network as well as the long-ranged dislocation stress fields. We also discuss how to extend this method to three spatial dimensions by invoking the full dislocation density tensor.

DOI: 10.1103/PhysRevB.76.094109 PACS number(s): 61.72.Bb, 81.10.Jt, 61.72.Lk

I. INTRODUCTION

Upon undergoing a severe plastic deformation, many metals and alloys display interesting microstructural evolution processes involving collective motion of dislocations at elevated temperatures.[1] The elastic energy stored during cold working is released on annealing via three main processes: recovery, recrystallization, and grain coarsening. Recovery is the process during which dislocations rearrange to form lower energy configurations, while recrystallization refers to the subsequent formation and migration of high-angle grain boundaries. Upon impingement of the recrystallized grains, grain coarsening takes over. These processes, driven by the relief of deformation stresses, affect several important microstructural features, including grain size and orientation (texture). Fundamentally, we would like to develop quantitative models which would predict the resulting post-recrystallization microstructure from the knowledge of the plastic deformation and material properties. From a theoretical perspective, this is a tall order: Any physically based description of the recrystallization phenomenon necessarily involves a seamless integration of processes across a multitude of length and time scales, ranging from the motion of isolated dislocations on the atomic scale up to the mesoscale dynamics of interacting dislocation ensembles. The aim of this paper is somewhat less ambitious in that our goal is to develop a mesoscale framework, which incorporates several key microscopic features of the process, for studying this collective phenomenon. In particular, our focus is on elucidating the growth morphologies of an isolated grain and relating them to the spatial features and heterogeneities in the dislocation network.

On the experimental side, several investigations have been carried out to describe the recrystallization kinetics in a variety of industrial and model alloys.[2–9] Modeling of the recrystallization has traditionally been based on microstructural representations of the cell/subgrain structure or the dislocation density. Fundamental interest in recrystallization has led to analytical models which could predict overall recrystallization kinetics and textures.[10–15] A model for recrystallization kinetics based on several physical parameters, such as grain-boundary mobility, average dislocation density, and grain size for interstitial-free steel, was proposed by Ye *et al.*[16] This model could capture the effect of the percentage of cold working on recrystallization kinetics. However, the abnormal growth seen in the recrystallization process and the irregular growth were not captured by this model. Indeed, the *in situ* experiments of Schmidt *et al.*[5] have clearly demonstrated that the growth morphology of an isolated grain can be highly irregular due to heterogeneities in the local dislocation density. Zurob *et al.*[17] proposed a model which could predict the recrystallization incubation time and the critical strain. It is noteworthy that the models discussed above are mean-field type in the sense that they do not explicitly track the morphology of evolving grains or the spatially heterogeneous dislocation distribution.

Microscopically, plastic deformation and concomitant dislocation motion have been studied at different levels of spatial and temporal resolutions. At the highest resolution, dislocation motion in pure metals and alloys has been elucidated by means of molecular dynamics simulations.[18–26] These studies have yielded a plethora of information regarding, e.g., dislocation core structure, the mobility of isolated dislocations, and the interaction between a relatively small number of dislocation loops. By integrating out the atomic degrees of freedom away from the dislocation core, a wide range of models for the overdamped motion of isolated dislocation lines and loops have been proposed over the years. Long-range interactions between dislocations are taken into account through linear elasticity theory, and short-range (core) interactions are incorporated through a set of constitutive relations for local dislocation reactions. Notable examples in this category include the recently introduced level-set method for studying dislocation interactions with particles,[27] kinetic Monte Carlo simulations of screw dislocation motion in bcc metals,[28] massive dislocation dynamics simulations of plasticity in metals and misfitting thin films,[29] and the phase-field methods of Refs. 30 and 31 for modeling individual dislocation loops as misfitting platelets. A feature shared by all these methods is that they resolve individual dislocation lines. These models have, in turn, contributed to an improved understanding of, e.g., work hardening and dislocation-precipitate interactions. Further decreasing the spatial and temporal resolution, Rickman and co-workers have investigated spatially extended systems with large dislocation densities by invoking a spatially coarse-grained dislocation density tensor.[32] As will be discussed in detail below, the work described in this paper builds on and extends the coarse-grained dislocation density description introduced by Rickman and co-workers.

Coarse-grained computational models have also been employed to investigate recrystallization and grain growth phenomena. Kinetic Monte Carlo simulations of the Potts model,[33–35] cellular automata models,[36–38] and phase-field simulations of grain growth[39] have yielded a wealth of information about the kinetics of grain growth and coarsening during recrystallization. A common feature of these models (as well as of the analytical models discussed above), however, is that they do not explicitly incorporate the long-ranged dislocation stress fields; in fact, the local driving force for grain growth is taken to be proportional to the local dislocation density. While this feature is not crucial in cases where the dislocation strain fields are effectively screened, there are cases where the long-ranged dislocation strain fields have a strong influence on the morphology of the growing grains prior to impingement, as we will demonstrate below.

In this paper, we consider a system which is already in a recovered state, and a germ nucleus is present, which subsequently grows. We have considered several different spatial dislocation distributions, including uniformly random configuration, square and rectangular cell structures, and algebraically correlated distributions, and have studied the effect of the dislocation distribution on the growth kinetics and morphologies of the isolated recrystallized nucleus. It is noteworthy that the average dislocation density was kept constant, and thus the changes in the growth morphologies were due to the distinct spatial dislocation arrangements. The uniformly random distribution of dislocations corresponds to low stacking fault energy (SFE) materials in which the dislocations do not organize into subgrains and the nucleation site is visualized in terms of a relatively dislocation-free region in the vicinity of a grain boundary. In high SFE materials, on the other hand, dislocations align to form more ordered cellular structures, which we approximate as collections of rectangular dislocation walls. The nucleation site in this case is simply a subgrain which has a lower stored energy than the neighboring subgrains.[17] The nuclei then grow preferentially into the neighboring grains because they benefit from very mobile high-angle boundaries. Finally, while algebraically correlated dislocation structures are usually observed only at very low temperatures[40] and thus are not as relevant at elevated temperatures, it is of fundamental interest to study the interplay between the long-ranged dislocation strain fields and the correlated dislocation structure with regard to the growth kinetics.

The paper is organized as follows. Sec. II presents the theoretical approach based on the coarse-grained dislocation density and phase-field methods employed in this study, while Sec. III examines the growth morphologies of a recrystallized grain in uniformly random, cellular, and algebraically correlated dislocation networks. Sec. IV presents the results for recrystallization rate kinetics and Avrami coefficients, while Sec. V contains a brief discussion and conclusions. Finally, the Appendix outlines an extension of our approach to three spatial dimensions.

II. THEORETICAL APPROACH

In this work, we employ the phase-field method (PFM), together with a coarse-grained dislocation density description, to simulate the growth of an isolated recrystallized grain within a cold-worked matrix in two spatial dimensions. We begin by introducing the coarse-grained dislocation description.

A. Elasticity theory and coarse-grained dislocation description

From a thermodynamics perspective, the driving force for the growth of the recrystallized grain is the reduction of the local elastic energy. Microscopically, this energy can be written as a sum of two terms, one arising from the smooth long-ranged elastic strains (treated here within linear elasticity theory) and another from the dislocation cores:

$$F_D = \frac{1}{2}\int d^2\vec{r}\sigma^s_{ij}\varepsilon^s_{ij} + \sum_{i=1}^{N}\frac{G\vec{b}_i^2(\vec{r}_i)}{c}. \tag{1}$$

Here, σ^s_{ij} denotes the two-dimensional $(2d)$ stress tensor, ε^s_{ij} is the corresponding strain tensor, G is the shear modulus, $\vec{b}_i(\vec{r}_i)$ is the Burgers vector of the ith dislocation located at $\vec{r}=\vec{r}_i$, and c is a constant related to the dislocation core energy $E_b=\frac{G\vec{b}_i^2}{c}$.

Rather than resolving individual dislocations, we employ a coarse-grained dislocation density approach where we average the local microscopic dislocation density over a small coarse-graining area $\sim\ell^2$,

$$\vec{b}(\vec{r}) = \ell^{-2}\sum_j \vec{b}_j(\vec{r}_j). \tag{2}$$

Here, the restricted sum is over those dislocations j for which $|\vec{r}-\vec{r}_j|\leqslant\ell/2$. By construction, for a uniform dislocation distribution, $\vec{b}(\vec{r})=\text{const}$, while $\vec{b}(\vec{r})\approx 0$ for a collection of tightly bound dislocation dipoles. The length ℓ sets the spatial scale over which the coarse-grained dislocation density varies. Specifically, setting ℓ comparable to the crystalline lattice spacing recovers an atomistically sharp dislocation density, while increasing ℓ leads to progressively coarser descriptions where more and more of the finer scale details in the dislocation density have been averaged out. In this work, ℓ is chosen to be comparable to the width of the diffuse interface (discussed in Sec. II B) between the recrystallized grain and the matrix. This choice makes the dislocation density computationally tractable in the numerical implementation of the model. Physically, the effects of dislocation structures on scales smaller than ℓ cannot be accurately modeled with this method. Nevertheless, such an approach, pioneered by Rickman and co-workers,[32] allows one to investigate spatially extended systems with large dislocation densities. This approach has previously been employed by one of us in elucidating stress-driven instabilities in thin film growth and effects of mobile dislocations on spinodal decomposition in misfitting binary alloys.[41]

As is well known, dislocations distort the crystalline lattice and give rise to long-ranged elastic stress and strain fields.[42–44] In what follows, we will relate the spatially heterogeneous dislocation density to the elastic stress fields it generates. We begin by noting that the dislocations can be characterized based on their Burgers vector $\vec{b}$, which is related to the elastic displacement field $\vec{u}^s(\vec{r})$ via the so-called closure failure $\oint_{\partial S} d\vec{u}^s = \sum_{m=1}^{N} \vec{b}_m$, where the integration contour encloses N dislocation cores. Introducing the deformation tensor $\omega_{ji} \equiv \partial u_i^s / \partial x_j$ and employing Green's theorem allows us to rewrite the closure failure as

$$\oint_{\partial S} du_i^s = \oint_{\partial S} \omega_{ji}\, dx_j = \sum_{m=1}^{N} b_{m;i} \tag{3}$$

or

$$\int_S d^2\vec{R}\, \epsilon_{kj} \nabla_k \omega_{ji} = \sum_{m=1}^{N} b_{m;i}, \tag{4}$$

where ϵ_{ik} denotes the $2d$ antisymmetric tensor with components $\epsilon_{xx} = \epsilon_{yy} = 0$ and $\epsilon_{xy} = -\epsilon_{yx} = 1$, and the summation over repeated indices is implied. Upon taking S to be equivalent to the coarse-graining area ℓ^2 centered at $\vec{r}$ and defining the coarse-grained deformation tensor via $\ell^2 \omega_{ji}^{CG}(\vec{r}) \equiv \int_S d^2\vec{R}\, \omega_{ji}(\vec{r} - \vec{R})$, we finally obtain the sought-after relation between ω_{ji}^{CG} and $\vec{b}(\vec{r})$, namely,

$$\epsilon_{kj} \nabla_k \omega_{ji}^{CG} = b_i(\vec{r}). \tag{5}$$

Since the characteristic rate of grain growth during recrystallization is very small compared to the speed of sound, it is safe to assume that elastic stresses equilibrate essentially instantaneously, thus becoming slaved to the slowly evolving dislocation distribution. In $2d$, the mechanical equilibrium equations are fulfilled automatically if the stress tensor is written as

$$\sigma_{ij}^s = \epsilon_{ik} \epsilon_{jl} \nabla_k \nabla_l \chi, \tag{6}$$

where $\chi(\vec{r})$ is the so-called Airy stress function.[45] Within linear elasticity, the strain ε_{ij}^s is related to the stress via

$$\varepsilon_{ij}^s = \frac{1}{2\mu} \sigma_{ij}^s - \frac{\lambda}{4\mu(\lambda + \mu)} \delta_{ij} \sigma_{kk}^s. \tag{7}$$

Here, Young's modulus is related to μ and λ via $Y_2 = \frac{4B\mu}{B+\mu}$, the Poisson ratio $\sigma_2 = \frac{B-\mu}{B+\mu}$, and the bulk modulus $B = \lambda + \mu$. Now, substituting for the Young's modulus, Poisson ratio, and bulk modulus in Eq. (7), we obtain

$$\varepsilon_{ij}^s = \frac{\sigma_2 + 1}{Y_2} \sigma_{ij}^s - \frac{\sigma_2}{Y_2} \delta_{ij} \sigma_{kk}^s. \tag{8}$$

Substituting Eq. (6) in Eq. (8) yields

$$\varepsilon_{ij}^s = \frac{\sigma_2 + 1}{Y_2} \epsilon_{ik} \epsilon_{jl} \nabla_k \nabla_l \chi - \frac{\sigma_2}{Y_2} \delta_{ij} \nabla^2 \chi. \tag{9}$$

Finally, applying $\epsilon_{ik} \epsilon_{jl} \nabla_k \nabla_l$ on either side of Eq. (9) and employing the relation $\varepsilon_{ij}^s = (\omega_{ji}^{CG} + \omega_{ij}^{CG})/2$ yields

$$\frac{1}{Y_2} \nabla^4 \chi = \epsilon_{ik} \nabla_i b_k(\vec{r}) = \nabla_x b_y(\vec{r}) - \nabla_y b_x(\vec{r}). \tag{10}$$

For a given $\vec{b}(\vec{r})$, solving the biharmonic equation above thus yields the Airy stress function $\chi(\vec{r})$, which can then be differentiated as in Eq. (6) to yield the components of the elastic stress tensor.

Written in terms of $\chi(\vec{r})$, the stored elastic energy due to dislocations is given by

$$F_D = \frac{1}{2Y_2} \int d^2\vec{r} (\nabla^2 \chi)^2 + \int d^2\vec{r} \left(\frac{G\vec{b}^2}{c} + e_0 \right). \tag{11}$$

Here, a constant elastic energy of magnitude, e_0, is added to the total energy to account for the presence of tightly bound dislocation dipoles, which exist within the coarse-graining area. Additionally, we have cast the elastic energy in Eq. (11) in a nondimensional form by measuring spatial lengths in units of L (to be specified later), gradients and derivatives in units of L^{-1}, the Burgers vector density in units of b_0/ℓ^2, and the Airy stress function in units of $L^3 b_0 Y_2 / \ell^2$. Consequently, the elastic energy in Eq. (11) is measured in units of $L^4 b_0^2 Y_2 / \ell^4$, while the dimensionless shear modulus is given by $G\ell^2/(L^2 Y_2)$.

B. Phase-field method

Several excellent papers exist on the application of the PFM to various microstructural evolution problems; see, e.g., Refs. 46–48. As usual, we introduce a scalar order parameter (OP) $\psi(\vec{r})$, which distinguishes between the recrystallized phase ($\psi = 1$) from the matrix ($\psi = -1$). The interface (i.e., grain boundary) is identified with the level set $\psi = 0$. Within the phase-field formalism, the total free energy of the system is now written as

$$F = F_\psi + \int d^2\vec{r} \left[\frac{(\nabla^2 \chi)^2}{2Y_2} + \frac{G\vec{b}^2}{c} + e_0 \right] g[\psi(\vec{r})], \tag{12}$$

where

$$F_\psi = \int d^2\vec{r} \left[\frac{1}{2} W^2 (\nabla \psi)^2 - \frac{\psi^2}{2} \left(1 - \frac{\psi^2}{2} \right) \right]. \tag{13}$$

Here, the functional form for $g(\psi)$ is dictated by the requirement that the equilibrium OP values are not shifted by the coupling to the dislocation elastic energy, implying that $dg/d\psi|_{\psi=\pm 1} = 0$.[49] A mathematically convenient choice adopted in this work is $g(\psi) = \psi^3/3 - \psi$; other choices are also possible. W is a parameter related to the thickness of the

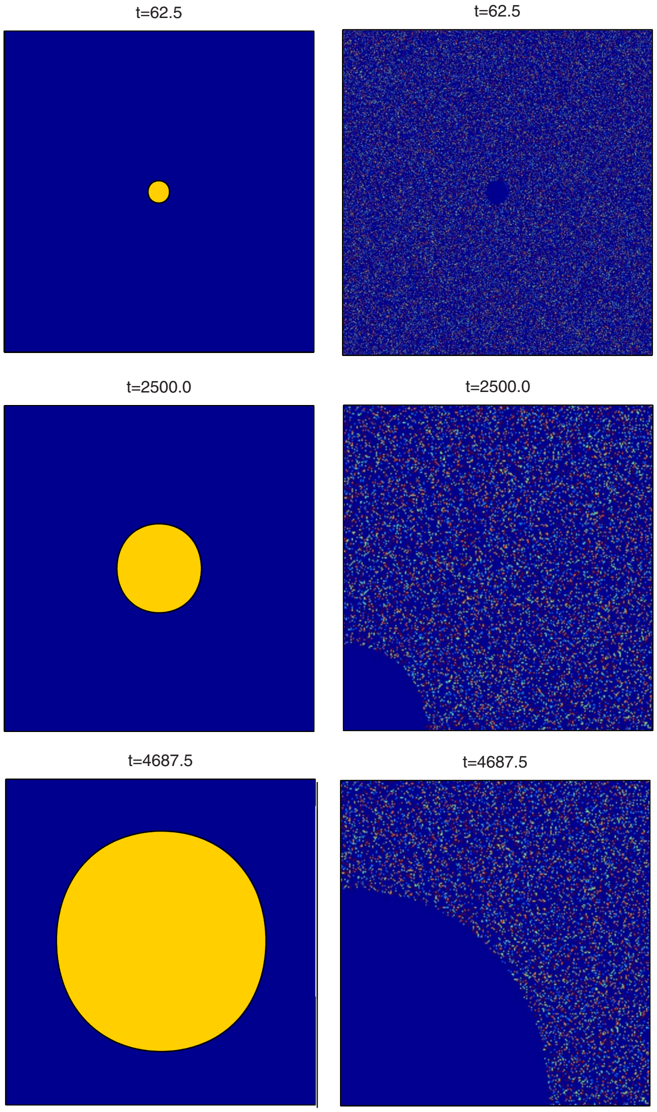

FIG. 1. (Color online) Snapshots of the growing recrystallization grain and (initially) uniformly random spatial distribution of dislocations. The figures on the left correspond to the evolution of the recrystallized grain, and those on the right correspond to the dislocation distribution. (Note that the dislocation plot corresponding to time $t=62.5$ shows the dislocation distribution for the entire system, while the subsequent dislocation plots display only the top quadrant for clarity.) In the morphology plots, yellow (gray) corresponds to the growing grain and blue (black) to the matrix. In the dislocation plots, red and pink correspond to $b_x=1$ and $b_x=-1$, and light blue and light green correspond to $b_y=1$ and $b_y=-1$, respectively.

interface and the surface tension between the two phases. The dynamical equation for the order parameter is given by

$$\frac{\partial\psi(\vec{r},t)}{\partial t} = -\Gamma\frac{\delta F(\psi\{\vec{r}\})}{\delta\psi(\vec{r})} = -\Gamma[W^2\nabla^2\psi + \psi - \psi^2 - g'(\psi)f_{el}], \tag{14}$$

where

$$f_{el} \equiv \frac{[\nabla^2\chi(\vec{r})]^2}{2Y_2} + \frac{G\vec{b}^2(\vec{r})}{c} + e_0 \tag{15}$$

denotes the local (dimensionless) elastic energy density. Here, Γ denotes the order parameter mobility [related to the mobility of the interface between the recrystallized and the cold-worked material (see below)], which, in principle, can be obtained from, e.g., molecular dynamics simulations.[50] In this work, we will consider an isotropic mobility in order to elucidate the effect of spatially heterogeneous dislocation distributions on grain growth; extension to an anisotropic Γ is straightforward and will be considered in a separate publication.[51] Typically, a Gaussian noise term consistent with the fluctuation-dissipation theorem is added to Eq. (14) to guarantee that the system approaches a thermodynamic equilibrium asymptotically. While such a noise term is crucial to facilitate nucleation, it has little effect on the subsequent growth of the grain. Thus, we have not included it in this work. Finally, the equations of motion for the dislocation densities are given by

$$\frac{\partial b_x(\vec{r},t)}{\partial t} = (m_g\nabla_x^2 + m_c\nabla_y^2)\frac{\delta F}{\delta b_x} - (1+\psi)b_x,$$

$$\frac{\partial b_y(\vec{r},t)}{\partial t} = (m_c\nabla_x^2 + m_g\nabla_y^2)\frac{\delta F}{\delta b_y} - (1+\psi)b_y, \tag{16}$$

where m_g and m_c denote dislocation glide and climb mobilities, respectively. The terms involving spatial gradients in Eq. (16) account for the glide and climb dynamics of the dislocation network in response to the long-ranged Peach-Koehler forces between the dislocations,[41] while the relaxational terms account for the dislocation–grain-boundary interactions, as discussed below. Since we are interested in the recrystallization and not the recovery phase, we will assume that dislocation cell wall formation has proceeded to its completion and therefore set $m_g=m_c=0$. Hence, the equations of motion for the dislocation densities become

$$\frac{\partial\vec{b}(\vec{r},t)}{\partial t} = -(1+\psi)\vec{b}. \tag{17}$$

At this point, we assume that the dislocations are simply incorporated into the moving grain boundary, and do not consider the microscopic features of this process in more detail. In particular, as soon as the grain boundary "sweeps" past a dislocation located at $\vec{r}$ [implying a change, $\psi(\vec{r})=-1\rightarrow\psi(\vec{r})=1$], it becomes incorporated (i.e., absorbed) into the grain boundary and no longer contributes to the overall elastic energy. This model is in accordance with recent experimental results, which demonstrate that "random" grain boundaries are capable of absorbing swept dislocations efficiently, while the migration of special boundaries (e.g., symmetric tilt boundaries) can be retarded by the presence of dislocations, not yet absorbed, being "dragged" along by the grain boundary (GB).[52] It is noteworthy that molecular dynamics simulations can be employed to elucidate the atomic scale processes occurring during dislocation-GB interactions.[53,54]

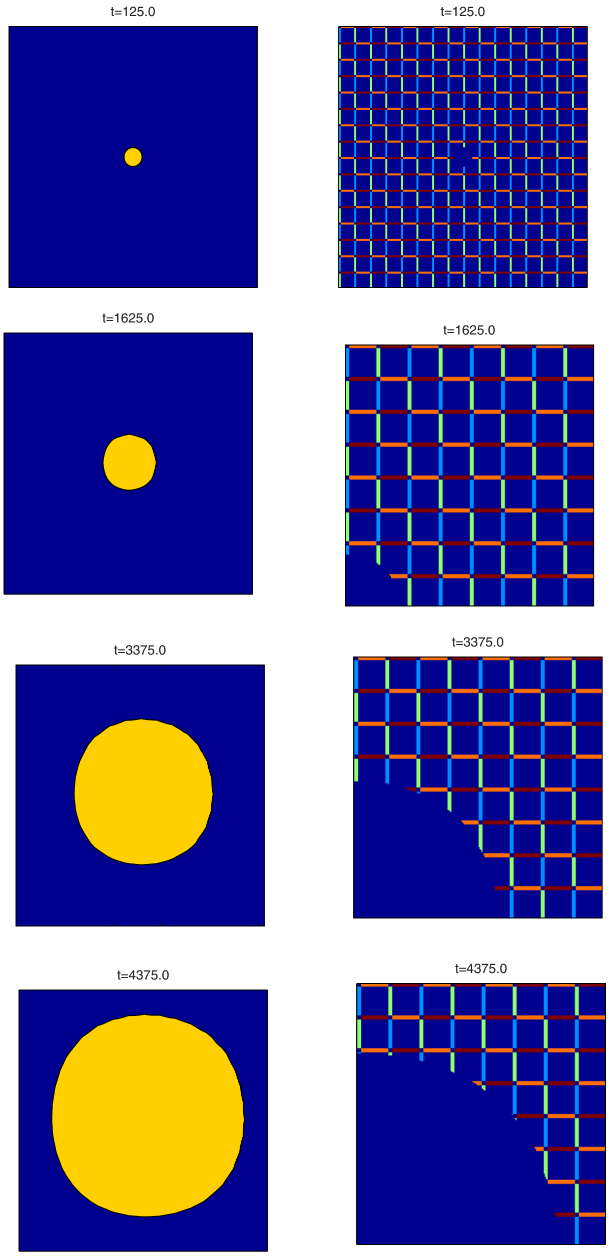

FIG. 2. (Color online) Morphological evolution for square cell structure and the corresponding dislocation distribution. Figures on the left correspond to the growing recrystallized grain, and those on the right to the dislocation distribution. In the morphology plots, yellow (gray) corresponds to the growing grain and blue (black) to the matrix. In the dislocation plots, red and pink correspond to $b_x=1$ and $b_x=-1$, and light blue and light green correspond to $b_y=1$ and $b_y=-1$, respectively. (Note that the first dislocation plot shows the dislocation distribution for the entire system, while the subsequent dislocation plots display only the top quadrant for clarity.)

To summarize, the OP evolves according to Eq. (14) and the dislocation density according to Eq. (17), and the elastic fields relax instantaneously; they are obtained by solving Eq. (10).

Interface equation of motion. It is instructive to derive the equation of motion for a gently curved interface via projection techniques. Following Ref. 46, we adopt a local (u,s) coordinate system, where u and s denote coordinates normal and tangent to the interface located at $\psi=0$, respectively. For a gently curved interface ($\kappa W \ll 1$, where κ denotes the local interface curvature), $\psi \approx \psi_{eq}(u-Vt)$, where $\psi_{eq}(x) = -\tanh(x/W\sqrt{2})$ and V denotes the local interface normal velocity. The Laplacian in this limit, written in terms of u and s becomes $\nabla^2 \approx \partial^2/\partial u^2 + \kappa\partial/\partial u + \partial^2/\partial s^2$.[46] Hence, Eq. (14) becomes

$$-V\frac{d\psi_{eq}}{du} = \Gamma\left[\psi_{eq} - \psi_{eq}^3 + W^2\frac{d^2\psi_{eq}}{du^2}\right] + \Gamma\left[W^2\kappa\frac{d\psi_{eq}}{du} - g'(\psi_{eq})f_{el}\right], \qquad (18)$$

where f_{el} denotes the local (dimensionless) elastic energy density. By construction, $\psi_{eq} - \psi_{eq}^3 + W^2 d^2\psi_{eq}/du^2 = 0$. Now, multiply both sides by the sharply peaked function $d\psi_{eq}/du$ and integrate over u to yield

$$-V\sigma = \Gamma\kappa W^2\sigma - \frac{4}{3}\Gamma f_{el;int} \qquad (19)$$

or

$$V = -\Gamma\left[W^2\kappa - \frac{4}{3\sigma}f_{el;int}\right], \qquad (20)$$

where $\sigma \equiv \int_{\infty}^{\infty} du(d\psi_{eq}/du)^2 = 2\sqrt{2}/(3W)$. In the above equations, we have employed the fact that $\int g'(\phi_{eq})d\psi_{eq}/du = 4/3$. Physically, Eq. (20) states that the interface moves in response to two thermodynamic forces—curvature κ and local elastic energy density at the interface $f_{\mathrm{el};int}$. As the interface propagates, dislocations are eliminated and their elastic fields no longer contribute to f_{el}. In our formulation, it is also evident that the driving force is truly nonlocal, as the singular stress fields are obtained by solving the biharmonic equation for the Airy stress function. It is noteworthy that the above analysis breaks down for sharply curved interfaces for which $\kappa W = \mathcal{O}(1)$, and the local normal velocity of the interface is no longer proportional to the curvature. Even in this limit, however, the phase-field model provides a physically reasonable (albeit qualitative) description of the interface dynamics.

We now explore this model for the recrystallization process. To this end, we begin with a small nucleus of the recrystallized phase (as it is indicated in experiments that a cell/subgrain which is already present in the cold-worked material acts as the nuclei) about 0.3% the size of the system, which is a uniform grid of 512×512 with grid spacing $\Delta x = 1.0$. Time is measured in units of Γ^{-1}, while length scales were measured in terms of the interface width $\hat{W}$ such that $W = \hat{W}/L = 1$. Explicit Euler integration is used with the (dimensionless) time step $\Delta t = 0.01$. Spatial derivatives were obtained using finite differencing, and the Airy stress function χ was resolved in Fourier space. A total of 57 344 (about 21%) dislocations were used, and the magnitude of the Burgers vector density was taken to be 1.0. The Burger's vector direction of the dislocations were taken to be either along the x axis or the y axis, as specified below. The total number of

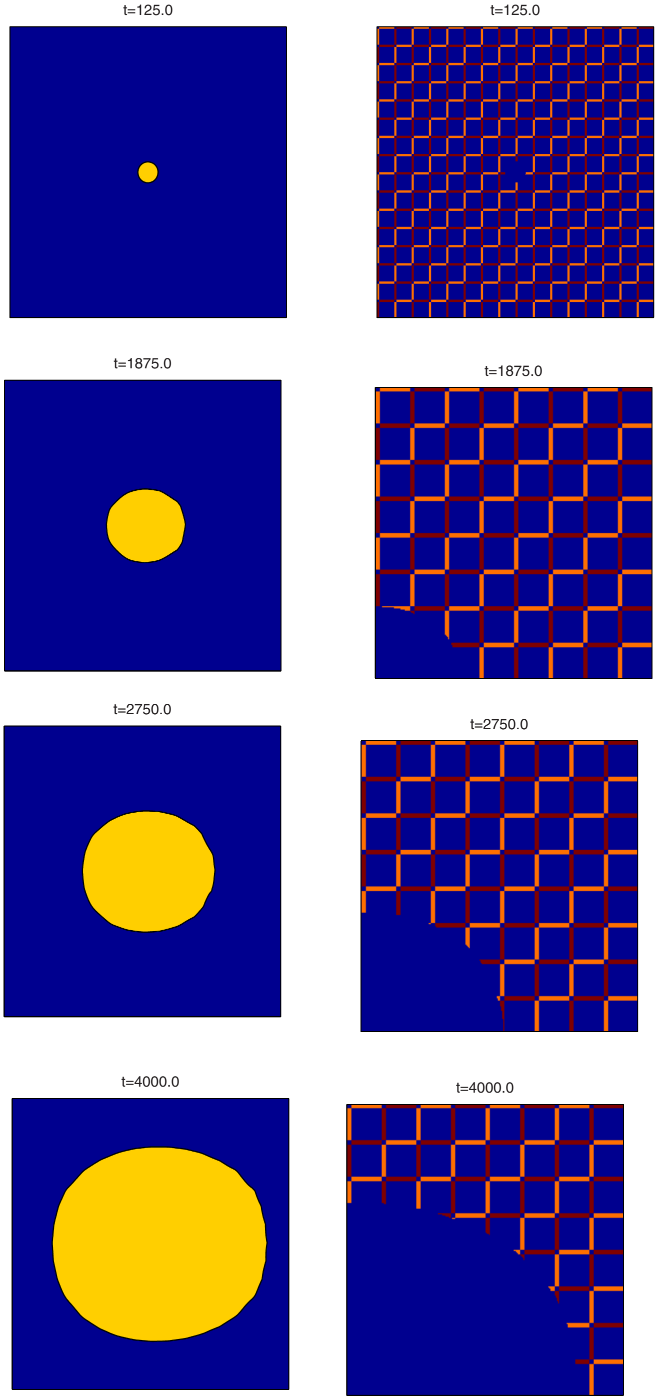

FIG. 3. (Color online) Morphological evolution for square cell structure whose walls are made up of dislocations with Burgers vector $b_x=\pm 1$. Figures on the left correspond to the morphology of the growing recrystallized grain and those on the right to the dislocation distribution. In the morphology plots, yellow (gray) corresponds to the growing grain and blue (black) to the matrix. In the dislocation plots, red and pink correspond to $b_x=1$ and $b_x=-1$. (Note that the first dislocation plot shows the dislocation distribution for the entire system, while the subsequent dislocation plots display only the top quadrant for clarity.)

dislocations was kept constant in the simulations in order to assess the role of spatial dislocation distribution on growth morphologies. The following parameters were employed in all the simulations reported here (unless stated otherwise): $c=1.0$, $G=0.075$, $e_0=0.04$, and $Y_2=1.25$. The specific values for these three parameters were chosen such that the core energy term and the long-ranged elastic part contribute approximately equal amounts to the free energy in Eq. (11) for an isolated dislocation of magnitude $b_{x/y}=\pm 1$. Second, the value of e_0 was chosen to be sufficiently large so as to drive the slow growth of the grain in the case where the coarse-grained dislocation density is set equal to zero. Finally, if we take $\hat{W}=\ell=100$ nm, the effective dislocation density becomes $\rho\sim 10^{14}$ m^{-2} for these choices of parameters. While the quantitative results are affected by the specific choice of parameters, the growth morphologies reported below were found to be insensitive with regard to the parameters.

III. SIMULATION RESULTS: GROWTH MORPHOLOGIES

A. Uniformly random dislocation distribution

In the case of low stacking fault energy materials, the dislocations at the end of the recovery phase do not form well-defined cell/subgrain structures and are approximately uniformly randomly distributed. To study grain growth in such systems, numerical simulations were carried out for cases with dislocation Burgers vectors along the x axis and also along both x and y axes. In the case where dislocation Burgers vectors along the x axis were used, the number of dislocation with positive and negative Burgers vectors was set to 28 672 each. On the other hand, when dislocations with Burgers vectors along both x and y axes were used, 14 336 dislocations were used for each of the different kinds, namely, dislocations with Burgers vectors along the positive and negative x axes $(b_x=\pm 1)$ and Burgers vectors along the positive and negative y axes $(b_y=\pm 1)$. Figure 1 shows the growth of the recrystallized phase when dislocations whose Burgers vector is along both the x and y directions were distributed in a uniformly random fashion. The snapshots in the left panel of Fig. 1 correspond to the morphology of the growing recrystallized phase, while the snapshots in the right hand panel correspond to the instantaneous dislocation distribution. From the snapshots, we can see that dislocations are removed from the growing recrystallized grain, resulting in a dislocation-free material. Note that the dislocation plot corresponding to time $t=62.5$ shows the dislocation distribution for the entire system, while the subsequent dislocation plots display only the top quadrant for clarity. As the dislocations are randomly distributed in this case, the recrystallized nucleus experiences similar driving forces in all directions, and hence the growth is isotropic (i.e., circular). It is also interesting to note that if the dislocation of one type and sign were employed, say, $b_x=1$, the morphology of the growing grain remained isotropic.

B. Cellular structures

Optical measurements done with aluminum and high stacking fault systems[7,55] have shown that dislocations can

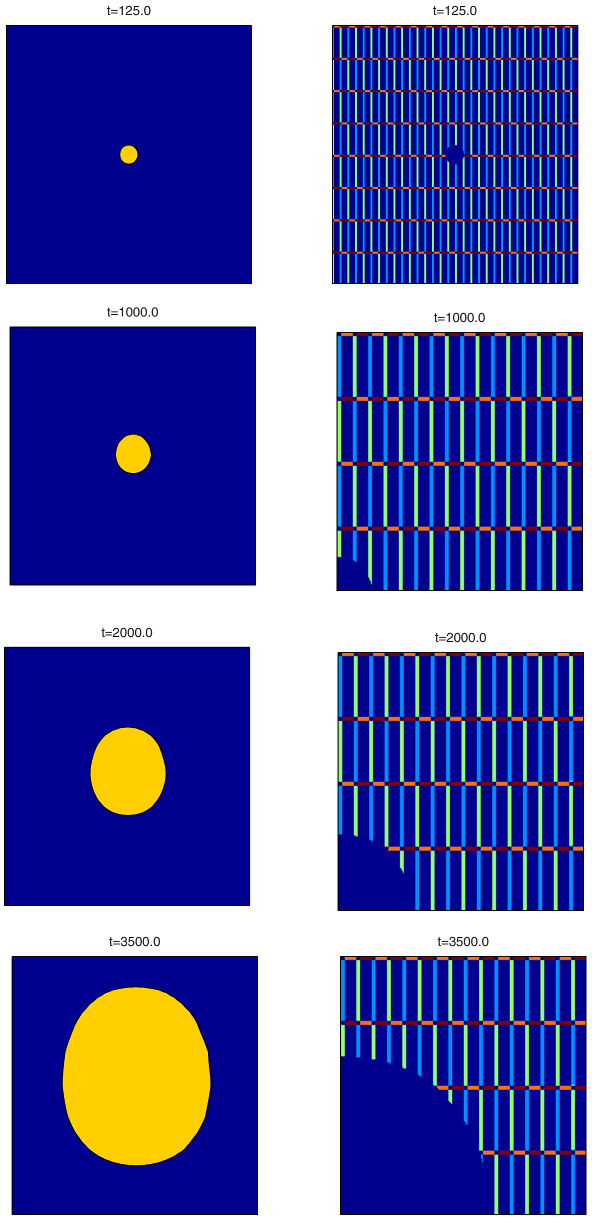

FIG. 4. (Color online) Morphological evolution of the recrystallized grain with dislocations stacked to form a rectangular cell structure. Figures on the left correspond to the growing recrystallized grain and those on the right to the dislocation distribution. In the morphology plots, yellow (gray) corresponds to the growing grain and blue (black) to the matrix. In the dislocation plots, red and pink correspond to $b_x=1$ and $b_x=-1$, and light blue and light green correspond to $b_y=1$ and $b_y=-1$, respectively. (Note that the first dislocation plot shows the dislocation distribution for the entire system, while the subsequent dislocation plots display only the top quadrant for clarity.)

evolve to form well-defined cells and cell walls; these cells may have either definite or irregular shapes.[40] In order to investigate the effect of ordered dislocation walls on grain growth, we carried out simulations with dislocations arranged to form both square and rectangular cells.

1. Square cell structures

In the square cell distribution, we have employed four dislocations to form the wall segments around a mesh of 28×28 dislocation-free grid points, so a complete square cell consists of a total of 32×32 grid points. This was repeated for the entire system of 512×512. The dislocations with identical Burgers vectors, $b_x=1$, is stacked together to form a wall of the cell structure, and the wall on the opposite side is formed by stacking dislocations with Burgers vector $b_x=-1$. The other two walls of the square cell are made by stacking $b_y=1$ for one wall and $b_y=-1$ for the other wall. The number of dislocations of each kind employed to form walls is 14 336, and the total number of dislocation with all four types is 57 344. While the net local Burgers vector in any region along the walls (other than the junctions) is nonzero, the overall Burgers vector for the entire system (as well as each individual square) is zero. Hence, the dislocation stress fields remain unscreened within a single cell, and they become effectively screened beyond this point. It is also noteworthy that the dislocations in this arrangement correspond to dislocation pileup segments rather than effective small-angle grain boundaries.

Figure 2 shows the morphological evolution of the recrystallized grain in an environment where dislocations were arranged as discussed above. In this case, we find that the growth morphology is still approximately isotropic despite the presence of regular dislocation pileups, which provide a larger driving force along the cell wall directions. In contrast, irregular (i.e., anisotropic) growth is observed if all dislocations comprising the walls have a Burgers vector $b_x=\pm1$. This is shown in Fig. 3, where a highly anisotropic growth pattern emerges. In this case, the dislocations are arranged in such a way that while the net Burgers vector is zero, all cell wall segments are made up from dislocations with the same Burgers vector ($b_x=1$ or $b_x=-1$); successive cell wall segments correspond to opposite b_x. Thus, the walls aligned in the x directions correspond to dislocation pileups, while the walls in the y direction can be viewed as grain boundaries. Although the effective dislocation density is the same in the x and y directions, the elastic driving force for growth in the x direction is much more pronounced than that in the y direction, and anisotropic growth ensues.

It is interesting to note that if the cell walls are constructed from dislocation dipoles, the growth morphology becomes isotropic (i.e., circular), as in the uniformly random case. Additionally, the growth rate of the grain was smaller than that in the uniformly random case for the same average dislocation density. These observations can be rationalized by recognizing that the effective elastic driving force for recrystallization is greatly reduced in the dipole cell wall case as the dislocation strain fields effectively cancel at very short distances. This reduced driving force, together with surface tension, promotes circular growth.

2. Rectangular cell structures

In light of the observation of irregular growth in the square cell wall system, we have investigated the effect of increased anisotropy in the dislocation distribution on grain growth by arranging the dislocations to form the cell walls of

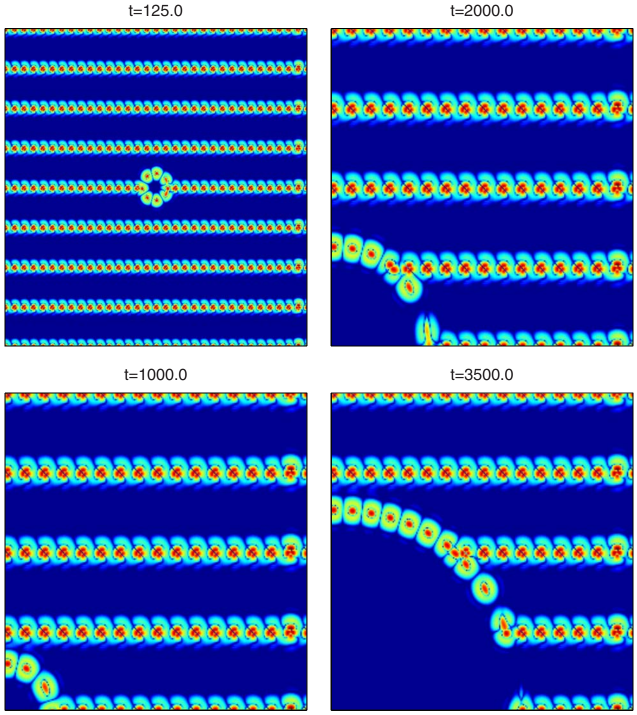

FIG. 5. (Color online) Stored elastic energy (logarithmic scale) for the dislocation distribution from Fig. 4. Blue (black) is the region with lower elastic energy. (Note that the first dislocation plot shows the dislocation distribution for the entire system, while the subsequent dislocation plots display only the top quadrant for clarity.)

a rectangular mesh of 60×12 dislocation-free grid points. The walls are again made up of four dislocations stacked together such that the local net Burgers vector is nonzero, while the overall Burgers vector equals zero. For this configuration, the anisotropic growth is even more pronounced, as can be clearly seen in Fig. 4. Here, the initially circular nucleus evolves into an overall elongated structure. This mode of growth arises from the anisotropic elastic driving force, which favors growth along the two cell wall directions, leading to an anisotropic growth pattern. This is clearly seen by inspecting snapshots of the stored elastic energy in the system in Fig. 5, which show that the driving force is the largest along the two cell wall directions of the rectangular cell, with the largest driving force per unit interface length occurring in the y direction. Based on these results [as well as the interface equation of motion in Eq. (20)], we expect a recrystallized grain with an isotropic surface tension to preferentially grow in the direction(s) along which the stored elastic energy density per unit interface length is the largest.

In the case of the rectangular cell dislocation configuration, it is worthwhile to consider the effect of cell walls comprised of dislocation dipoles. For the same overall dislocation density, the recrystallized grain did not show any morphological heterogeneities but instead grew approximately as a circular grain, as in the square cell case. The changes in the cell structure, therefore, do not significantly affect the growth of recrystallized grain when the walls are made of dislocation dipoles. Again, this can be understood as a consequence of a reduced elastic driving force due to the cancellation of the dislocation strain fields; this reduction in f_{el}, together with surface tension, promotes more isotropic growth.

3. Checkerboard dislocation pattern

The studies of square and rectangular cell structures on the growing morphology of the recrystallized grain discussed above motivated us to investigate the effect of dislocation distribution made up of a combination of the above two cellular configurations. The specific configuration we chose, shown in the left panel of Fig. 6, consists of square cells where dislocations with $b_y = \pm 1$ were aligned either along the x axis (to form short grain-boundary segments) or the y axis (to form short pileup segments) in successive squares; such a configuration implies that the maximum driving force per unit interface length alternates in direction as the grain grows. The following parameters were employed for this simulation: $c=1.0$, $G=0.03$, $e_0=0.025$, and $Y_2=1.5$. In this case, the interface of the recrystallized grain evolves in a highly anisotropic and irregular manner, as shown in the right panel of Fig. 6. During the initial stages of growth, the recrystallized grain has the largest driving force approximately along the diagonal, and hence the growth is very fast in that direction. Once the localized dislocation aggregate ahead of the interface has been consumed, the largest driving force per unit length switches direction and is now found approximately along the other diagonal; hence, the interface displays a growth "spurt" in this direction.

Beyond some point, different parts of the growing interface experience a maximum driving force along different directions, and hence the growth proceeds in a highly irregular manner. It is interesting to note that during the initial stages, we have observed that protrusions from the growing interface sometimes shrink back once the driving force is locally exhausted at the interface. These observations bear a striking resemblance with the *in situ* experimental observations of irregular growth of an isolated growing grain in Ref. 5.

C. Algebraically correlated dislocation distribution

Finally, we will consider the effect of algebraically correlated dislocation distributions on recrystallization kinetics. Indeed, during plastic deformation at low temperatures, dislocations often form self-similar dislocation-rich cell walls separating dislocation-depleted cell interiors. To quantify the resulting spatial dislocation structures, Hahner *et al.*[40] employed the so-called box counting method to estimate the fractal dimension of the micrographs of the dislocation patterns formed in Cu single crystals. To this end, the number $N(\Delta x)$ of boxes with edge length Δx containing at least one pixel of a cell wall was determined, and a relation $N(\Delta x) \sim \Delta x^{-D_B}$ was established. Here, D_B is the so-called box counting dimension, which is obtained from the slope m of the double logarithmic plot of $N(\Delta x) \times \Delta x^2$ vs Δx as $D_B = 2 - m$. Hahner *et al.*[40] found that D_B increased with applied stress. For example, for an applied stress of 68.2 MPa, $D_B \approx 1.78 \pm 0.04$, while for a higher stress of 75.6 MPa, $D_B \approx 1.85 \pm 0.06$.

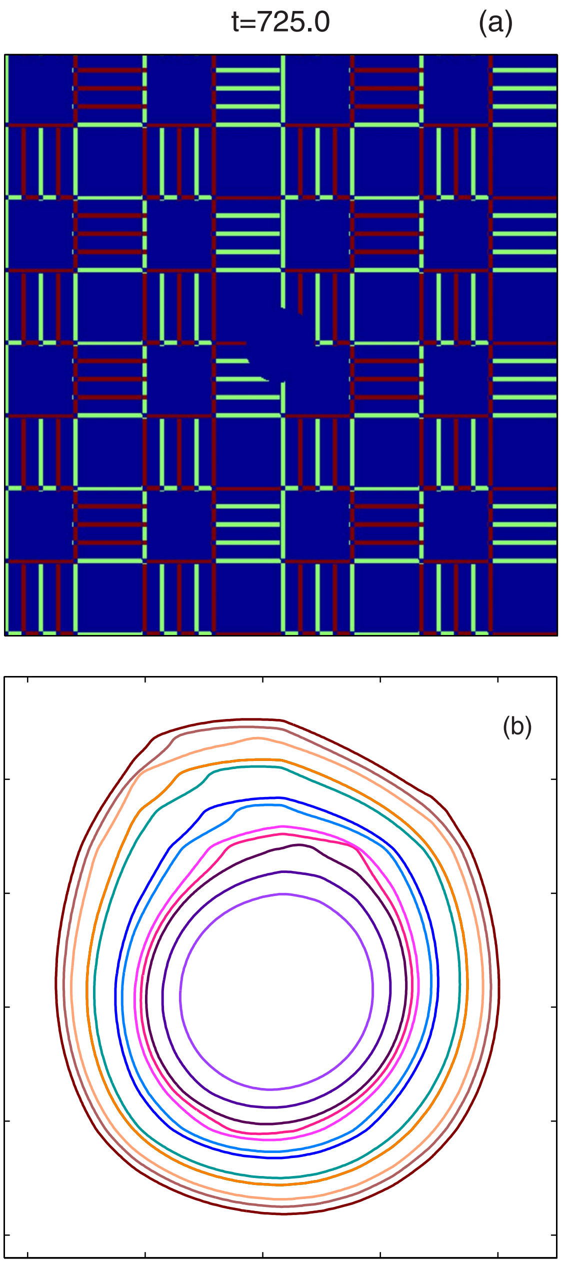

FIG. 6. (Color online) (a) Checkerboard dislocation network. (b) Sequence of interface positions during displaying irregular growth morphologies.

We have investigated the effect of such correlated networks by constructing dislocation distributions whose pair correlation function asymptotically satisfies $G(\vec{r},\vec{r}) = \langle b_i(\vec{r}) b_j(\vec{r}\,')\rangle \delta_{ij} \sim |\vec{r}-\vec{r}|^{-\eta}\delta_{ij}$, where $\eta = 2 - D_B$ in $2d$; specifically, we have considered the correlation coefficient value $\eta = 0.20$, which corresponds to $D_B = 1.8$. The spatially correlated dislocation distributions were generated by adapting the algorithm proposed by Makse *et al.*[56] to generate a sequence of random numbers with long-range algebraic correlations. Using the sequence of such algebraically correlated random numbers, we distributed 14 336 dislocations each with Burgers vectors $b_x = \pm 1$ and $b_y = \pm 1$, for a total of 57 344 dislocations.

Figure 7 shows snapshots of the morphology of the growing grain in a correlated dislocation distribution and the corresponding dislocation distribution. For these parameter values, the growing grain shows some heterogeneities, while the overall morphology remains isotropic. This is somewhat surprising in the light of the strongly heterogeneous elastic driving force, displayed in Fig. 8. Specifically, the observed heterogeneities are not sufficiently strong to induce anisotropic growth. Not surprisingly, if the nonlocal strains are eliminated, the resulting growth rates were smaller compared to the case with nonlocal strains. For a correlation coefficient in the range of 0.1–0.35, the growth rate is the same, while the morphology of the growing grain becomes rougher for correlation coefficients above ~0.25. For very high correlations, i.e., above 1.0, the distributions are similar to the uniformly random distribution discussed above, and the growth morphologies become isotropic again. We have not explored the effect of a correlation coefficient in the range of 0.7–1.0.

IV. SIMULATION RESULTS: RATE KINETICS AND AVRAMI COEFFICIENTS

To quantify the effects of the spatial dislocation distribution on recrystallization kinetics, we have measured the area fraction of the recrystallized phase versus time for the different dislocation distributions discussed above. This is shown in Fig. 9, and it displays several important features. First, all curves show two distinct regions, the first region where the growth rate is slow and the second one where a substantial amount of the cold-worked phase recrystallizes in a short time. The latter stage is characterized by grain coarsening, which is similar to the kinetics of normal grain growth. Second, the overall growth rate is much faster in the case of cellular structures (square and rectangular) than in the uniformly random and algebraically correlated distributions. This is due to the presence of effective dislocation pileups in the vicinity of the growth front, which provides a large driving force along specific directions, leading to faster local interface growth. On the other hand, a comparison of the uniformly random and algebraically correlated systems reveals that their growth rates are the same, even though for the algebraically correlated case, dislocation stress fields are not screened as effectively as they are in the uniformly random case.

A useful way to analyze the data is to try to fit it to the well-known Kolmogorov-Johnson-Mehl-Avrami equation[10,57,58]

$$\phi_A = 1 - \exp(-Bt^k), \tag{21}$$

where B and k are constants. To this end, the time dependent parameter ϕ_A (for the intermediate region of Fig. 9), which is the recrystallized area, is plotted in Fig. 10 using the Avrami format where $-\ln(1-\phi_A)$ is plotted as a function of time on log-log coordinates. As we begin with a heterogeneous nucleus being present, we have extracted the Avrami constant k from the data between $0.02 < \phi_A < 0.30$; the different k values are listed in Table I. In the case of a heterogeneous nucleation with constant radial growth, $k_{2D} = 2$. Not surprisingly, $k \approx 2$ for the uniformly random and algebraically cor-

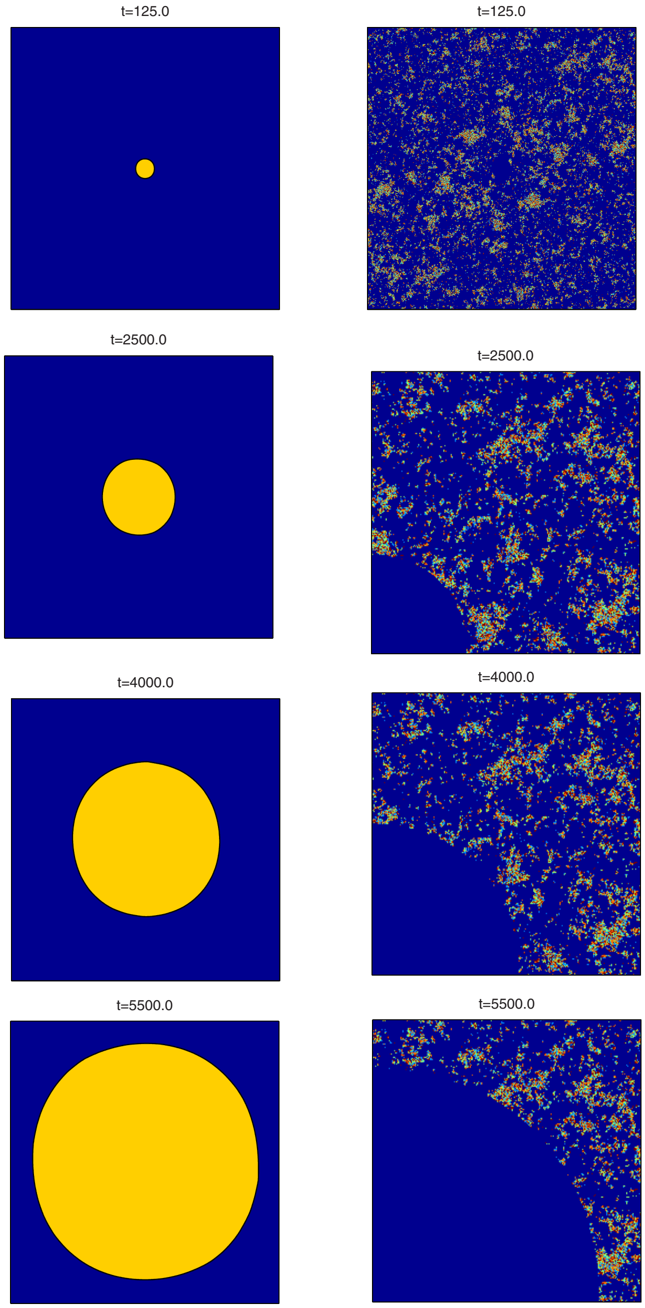

FIG. 7. (Color online) Morphologies for the growing grain for the algebraically correlated dislocation distribution and the corresponding dislocation distributions. Figures on the left correspond to the growing recrystallized grain and those on the right to the dislocation distribution. In the morphology plots, yellow (gray) corresponds to the growing grain and blue (black) to the matrix. In the dislocation plots, red and pink correspond to $b_x=1$ and $b_x=-1$, and light blue and light green correspond to $b_y=1$ and $b_y=-1$. (Note that the first dislocation plot shows the dislocation distribution for the entire system, while the subsequent dislocation plots display only the top quadrant for clarity.)

TABLE I. Avrami growth coefficient for various dislocation distributions. The error bars are estimated from exponential fits from a single run.

Dislocation distribution	Avrami constant	Error
Random	2.05	0.03
Square cell	1.74	0.07
Square cell dipoles	2.09	0.03
Rectangle cell	1.50	0.07
Correlated	1.93	0.05

related dislocation distributions, as well as for cellular cases where dislocation dipoles were used to form the cell walls. Indeed, the growth morphology was observed to be isotropic in these cases, similar to experimental growth morphologies during aluminum recrystallization.[59] However, in the cellular cases where dislocations of the same Burgers vector were stacked together to form the walls, the effective Avrami constant k was in the range of $1.50\pm0.07-1.74\pm0.07$, the lower values correspond to that of a rectangular cell structure. This difference in the growth kinetics can be attributed to the anisotropic growth of the recrystallized phase. The stored energy in these configurations are also highly anisotropic, and hence they influence the rate of growth of the recrystallized phase. More quantitatively, constant needlelike growth along one of the coordinate directions $(L_1\sim t)$ would yield $k=1$, while slower growth along the other axis $(L_2\sim t^{\alpha})$ would lead to $k=1+\alpha$. Here, we suspect that the effective Avrami coefficient $k<2$ is a manifestation of the small grain size compared to the dislocation cell size. Physically, we expect that the cellular wall cases would also lead to $k=2$ asymptotically once the grain size becomes much greater than the cell size. On the other hand, one may also speculate that the algebraically correlated dislocation distributions may lead to $k<2$ asymptotically, as the dislocation strain fields remain unscreened asymptotically and thus provide an effective grain size-dependent driving force. We plan to explore this scenario in future work.

V. DISCUSSION

In this work, we have developed a coupled dislocation density and phase-field method to model the isothermal recrystallization process as a phase transformation driven by the stored elastic energy in two spatial dimensions; in the Appendix, we demonstrate how to extend this method to three spatial dimensions by invoking the full dislocation density tensor. In the present work, dislocations are represented in two spatial dimensions in terms of a continuous Burgers vector field, and their contribution to the elastic energy density is explicitly incorporated. A key feature of our approach is that the driving force for grain growth becomes nonlocal in space due to the presence of long-ranged dislocation strain fields. We have employed the model to examine the influence of various spatially heterogeneous dislocation distributions, including uniformly random, cellular, and algebraically correlated ones on the growth morphology of an isolated recrystallized grain. In all three cases, the overall average dislocation density was kept constant, allowing us to assess and quantify the effect of spatial dislocation distribution on the growth morphologies.

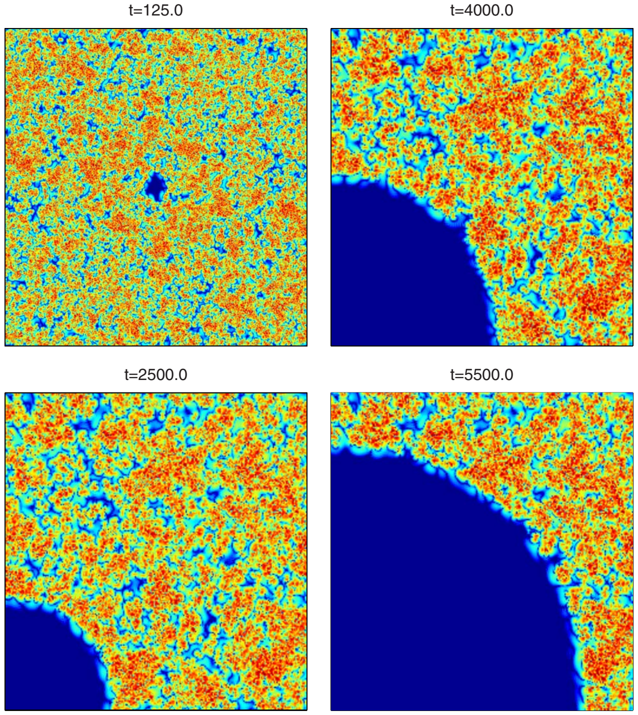

FIG. 8. (Color online) Stored elastic energy (logarithmic scale) for algebraically correlated dislocation distribution from Fig. 7. Blue (black) regions correspond to regions of lowest elastic energy. Red regions represent the maximum stored energy, and light blue and yellow stand for intermediate values of stored energy. (Note that the first dislocation plot shows the dislocation distribution for the entire system, while the subsequent dislocation plots display only the top quadrant for clarity.)

With regard to recrystallization, the results presented in this paper clearly establish the fact that the morphology of the growing recrystallized grain is strongly affected by the spatial features of the underlying dislocation network. In the uniformly random case, the growth morphology was found to be isotropic, reflecting the rather isotropic elastic driving force. However, in the case of cellular dislocation networks, the growth morphologies were anisotropic, similar to those observed in experiments. Here, the degree of anisotropy was related to the detailed structure of the walls: In cases where the walls comprised of dislocations with the same Burgers vector, the growth was markedly anisotropic, while in cases where the walls comprised of dislocation dipoles, more isotropic growth was observed. Thus, the degree of anisotropy could be traced to the local elastic driving force, which is sensitive to the degree by which nearby dislocations do or do not screen each other's stress fields. Finally, in the case of algebraically correlated dislocation networks, varying degrees of irregularity in the growth morphology were observed. In the case where dislocations of both types ($b_x = \pm 1$ and $b_y = \pm 1$) were employed, the growth was fairly isotropic. Interestingly, numerical experimentation has shown that when only dislocations with $b_x = \pm 1$ or $b_y = \pm 1$ are employed, the growth morphology becomes much more irregular. In future work, it will be of great interest to introduce an anisotropic interface mobility and/or surface tension and investigate the interplay between heterogeneous dislocation structures and anisotropic interface properties on growth morphologies. Specifically, we will investigate the interplay between statistically stored and geometrically necessary dislocations on growth morphologies. As a final note, we hope that the approach and results presented in this paper will catalyze more detailed experimental and theoretical studies into the effects of grain-boundary mobility and dislocation heterogeneities on grain growth.

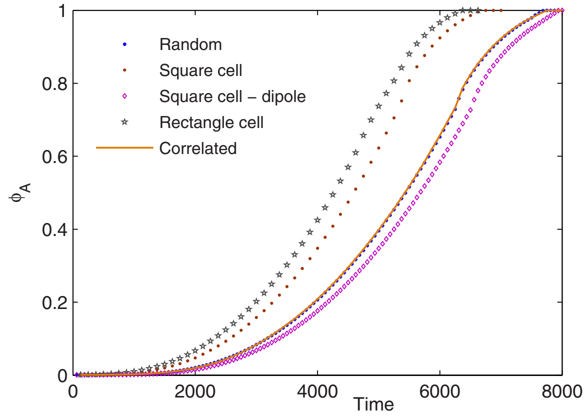

FIG. 9. (Color online) Area fraction of the recrystallized phase as a function of time.

ACKNOWLEDGMENT

This work has been supported by NSF-DMR Grant No. 0449184.

APPENDIX: MODEL IN THREE SPATIAL DIMENSIONS

The extension of our model to three spatial dimensions is straightforward. Instead of the two-component Burgers vector, we invoke the full dislocation density tensor $\rho_{ij}(\vec{r})$, where i and j denote the dislocation line and Burgers vector directions, respectively, coarse grained over a volume ℓ^3 centered at $\vec{r}$. Given an instantaneous dislocation configuration in an elastically isotropic and homogeneous material, the resulting stress tensor (in Fourier space) is explicitly given by

$$\hat{\sigma}_{ij}(\vec{q}) = K_{ijlk}(\vec{q})\hat{\rho}_{kl}(\vec{q}), \tag{A1}$$

where the tensor K_{ijkl} is given by[42]

$$K_{ijlk}(\vec{q}) = -\frac{\imath G q_m}{q^2}\left[\varepsilon_{ilm}\delta_{jk} + \varepsilon_{jlm}\delta_{ik} + \frac{2\varepsilon_{klm}}{1-\nu}\left(\frac{q_i q_j}{q^2} - \delta_{ij}\right)\right] \tag{A2}$$

and where $\imath \equiv \sqrt{-1}$. The driving force for recrystallization is again given by the stored elastic energy

$$F_D = \frac{1}{2}\int d^3\vec{r}\,\sigma^s_{ij}\varepsilon^s_{ij} + \int d^2\vec{r}\,\frac{G\rho_{ij}^2}{c}. \tag{A3}$$

The order parameter couples to the stored elastic energy as in the two-dimensional case, and the OP dynamics are given by Eq. (14). The dislocation density tensor evolves according to the simple relaxational kinetic equation given by

$$\frac{\partial\rho_{ij}(\vec{r})}{\partial t} = -(1+\psi)\rho_{ij}(\vec{r}). \tag{A4}$$

We are currently investigating the full three-dimensional growth kinetics of recrystallized grains based on the above approach and will report on it in a future publication.[51]

---

*sree@princeton.edu

†mhaataja@princeton.edu

[1] F. J. Humphreys and M. Hatherly, *Recrystallization and Related Annealing Phenomena* (Pergamon, Oxford, UK, 1996).

[2] E. Nes, Acta Metall. Mater. **43**, 2189 (1995).

[3] R. D. Doherty, D. A. Hughes, F. J. Humphreys, J. J. Jonas, D. Juul Jensen, M. E. Kassner, W. E. King, T. R. McNelley, H. J. McQueen, and A. D. Rollett, Mater. Sci. Eng., A **238**, 219 (1997).

[4] R. A. Vandermeer and D. Juul Jensen, Acta Mater. **49**, 2083 (2001).

[5] S. Schmidt, S. F. Nielsen, C. Gundlach, L. Margulies, X. Huang, and D. Juul Jensen, Science **305**, 229 (2004).

[6] D. E. Solas, C. N. Tomé, O. Engler, and H. R. Wenk, Acta Mater. **49**, 3791 (2001).

[7] R. V. Ramanujan, J. Mater. Sci. **35**, 2379 (2000).

[8] H. Jazaeri and F. J. Humphreys, Acta Mater. **52**, 3239 (2004); **52**, 3251 (2004).

[9] A. Belyakov, T. Sakai, H. Miura, R. Kaibyshev, and T. Tsuzaki, Acta Mater. **50**, 1547 (2002).

[10] M. Avrami, J. Chem. Phys. **7**, 1103 (1939); **8**, 212 (1940); **9**, 117 (1941).

[11] H. E. Vatne, T. Furu, R. Ørsund, and E. Nes, Acta Mater. **44**, 4463 (1996).

[12] F. J. Humphreys, Acta Mater. **45**, 4231 (1997).

[13] F. J. Humphreys, Acta Mater. **45**, 5031 (1997).

[14] P. J. Hurley and F. J. Humphreys, Acta Mater. **51**, 3779 (2003).

[15] M. Crumbach, M. Goerdeler, and G. Gottstein, Acta Mater. **54**, 3275 (2006); **52**, 3291 (2006).

[16] W. Ye, R. L. Gall, and G. Saindrenan, Mater. Sci. Eng., A **332**, 41 (2002).

[17] H. S. Zurob, Y. Bréchet, and J. Dunlop, Acta Mater. **54**, 3983 (2006).

[18] D. Rodney and G. Martin, Phys. Rev. Lett. **82**, 3272 (1999).

[19] T. Rasmussen, K. W. Jacobsen, T. Leffers, and O. B. Pedersen, Phys. Rev. B **56**, 2977 (1997).

[20] J. P. Chang, W. Cai, V. V. Bulatov, and S. Yip, Mater. Sci. Eng., A **309**, 160 (2001).

[21] M. de Koning, W. Cai, and V. V. Bulatov, Phys. Rev. Lett. **91**, 025503 (2003).

[22] J. Schiotz and K. W. Jacobsen, Science **301**, 1357 (2003).

[23] J. Marian, W. Cai, and V. V. Bulatov, Nat. Mater. **3**, 158 (2004).

[24] L. Olmsted, L. G. Hector, W. A. Curtin, and R. J. Clifton, Modell. Simul. Mater. Sci. Eng. **13**, 371 (2005).

[25] J. Marian and A. Caro, Phys. Rev. B **74**, 024113 (2006).

[26] L. Holian and P. S. Lomdahl, Science **280**, 2085 (1998).

[27] Y. Xiang, L.-T. Cheng, D. J. Srolovitz, and W. E, Acta Mater. **51**, 5499 (2003); Y. Xiang, D. J. Srolovitz, L.-T. Cheng, and W. E, Acta Mater. **52**, 1745 (2004).

[28] C. S. Deo and D. J. Srolovitz, Modell. Simul. Mater. Sci. Eng. **10**, 581 (2002).

[29] R. Madec, B. Devincre, and L. P. Kubin, Phys. Rev. Lett. **89**, 255508 (2002); K. W. Schwarz, *ibid.* **91**, 145503 (2003).

[30] Y. U. Wang, Y. M. Jin, A. M. Cuitino, and A. G. Khachaturyan, Acta Mater. **49**, 1847 (2001).

[31] D. Rodney, Y. Le Bouar, and A. Finel, Acta Mater. **51**, 17 (2003).

[32] J. M. Rickman and J. Vinals, Philos. Mag. A **75**, 1251 (1997); R. LeSar and J. M. Rickman, Phys. Rev. B **65**, 144110 (2002); **69**, 172105 (2004); J. M. Rickman and R. LeSar, Scr. Mater. **54**, 735 (2006).

[33] D. J. Srolovitz, G. S. Grest, and M. P. Anderson, Acta Metall. **34**, 1833 (1986).

[34] D. Raabe, Acta Mater. **48**, 1617 (2000).

[35] E. A. Holm and C. C. Battaile, JOM **53**, 20 (2001).

[36] C. H. J. Davies, Scr. Metall. Mater. **33**, 1139 (1995).

[37] D. Raabe, Mater. Sci. Forum **273-275**, 169 (1998).

[38] D. Raabe, Annu. Rev. Mater. Res. **32**, 53 (2002).

[39] L. Q. Chen and W. Yang, Phys. Rev. B **50**, 15752 (1994).

[40] P. Hahner, K. Bay, and M. Zaiser, Phys. Rev. Lett. **81**, 2470 (1998).

[41] M. Haataja, J. Müller, A. D. Rutenberg, and M. Grant, Phys. Rev. B **65**, 035401 (2001); **65**, 165414 (2002); M. Haataja and F. Leonard, *ibid.* **69**, 081201(R) (2004).

[42] T. Mura, *Micromechanics of Defects in Solids*, 2nd ed. (Kluwer Academic, Dordrecht, 1991).

[43] E. Kröner, Ergeb. Angew. Math **5**, 1 (1958).

[44] A. Acharya, J. Mech. Phys. Solids **49**, 761 (2001).

[45] L. Landau and E. M. Lifshitz, *Theory of Elasticity* (Pergamon, Oxford, 1986).

[46] K. R. Elder, M. Grant, N. Provatas, and J. M. Kosterlitz, Phys. Rev. E **64**, 021604 (2001).

[47] L. Q. Chen, Annu. Rev. Mater. Res. **32**, 113 (2002).

[48] W. J. Boettinger, J. A. Warren, C. Beckermann, and A. Karma, Annu. Rev. Mater. Res. **32**, 163 (2002).

[49] R. Kobayashi, Physica D **63**, 410 (1993).

[50] H. Zhang, M. Upmanyu, and D. J. Srolovitz, Acta Mater. **53**, 79 (2003); H. Zhang and D. J. Srolovitz, *ibid.* **54**, 623 (2006).

[51] S. Sreekala and M. Haataja (unpublished).

[52] D. A. Molodov, P. Konijnenberg, W. Hu, G. Gottstein, and L. S. Shvindlerman, Scr. Mater. **45**, 229 (2001).

[53] M. de Koning, R. J. Kurtz, V. V. Bulatov, C. H. Henager, R. G. Hoagland, W. Cai, and M. Nomura, J. Nucl. Mater. **323**, 281 (2003).

[54] M. Dewald and W. A. Curtin, Modell. Simul. Mater. Sci. Eng. **15**, S193 (2007).

[55] J. Gan, J. S. Vetrano, and M. A. Khaleel, ASME J. Eng. Mater. Technol. **124**, 297 (2002).

[56] H. A. Makse, S. Havlin, M. Schwartz, and H. E. Stanley, Phys. Rev. E **53**, 5445 (1996).

[57] A. Kolmogorov, Izv. Akad. Nauk SSSR, Ser. Fiz. **3**, 355 (1937).

[58] W. A. Johnson and P. A. Mehl, Trans. AIME **135**, 416 (1939).

[59] R. A. Vandermeer and D. Juul Jensen, Acta Mater. **49**, 2083 (2001).